Electronic Supplementary Information

Efficient photoredox conversion of alcohol to aldehyde and H_2 by heterointerface engineering of bimetal-semiconductor hybrids

Chuang Han,[ab] Zi-Rong Tang,[b] Junxue Liu,[c] Shengye Jin,[c] and Yi-Jun Xu*[ab]*

[a]State Key Laboratory of Photocatalysis on Energy and Environment, College of Chemistry, Fuzhou University, Fuzhou 350116, China

[b]College of Chemistry, New Campus, Fuzhou University, Fuzhou 350116, China

[c]State Key Laboratory of Molecular Reaction Dynamics, Dalian Institute of Chemical Physics, Chinese Academy of Sciences, Dalian, Liaoning 116023, China

**Corresponding authors. E-mail: sjin@dicp.ac.cn; yjxu@fzu.edu.cn*

Contents list

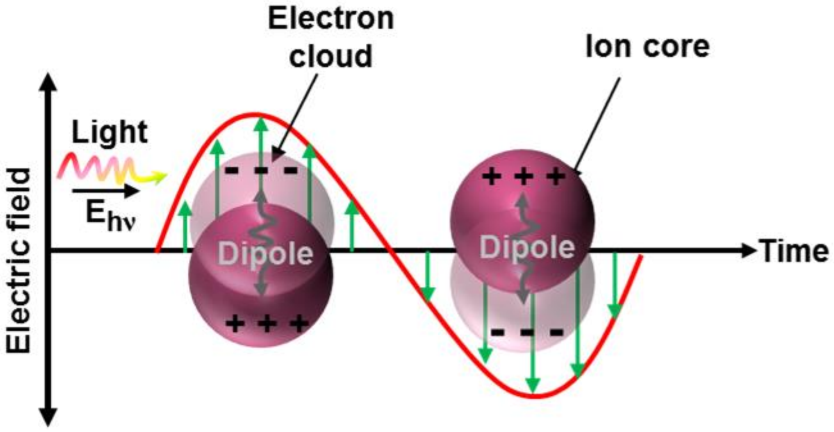

Scheme S1 Schematic illustration of the surface plasmon resonance (SPR) in metallic nanostructures induced by the electric field of incident light.

Note: As shown in **Scheme S1**, when metallic nanostructures are illuminated by light with a wavelength far exceeding their size, the electron will distribute asymmetrically, which decreases on one side of the nanostructure and increases on the other side (*i.e.*, polarization). During the process of electron density displacement, a Coulombic restoring force is established between the negative electrons and the positive nuclei, thereby leading to electron cloud oscillations relative to the ion core. When the photon frequency matches the natural frequency of the metal surface electrons oscillating, the photons are efficiently coupled with the resonant collective electrons and SPR occurs.[S1-S3]

Plasmonic metals are a class of fascinating materials with unique optical features characterized by their strong interaction with resonant photons and intense local electromagnetic field near the surface through the excitation of SPR.[S1, S4] The most researched plasmonic metals are Au and Ag, which have distinct and well-defined SPR absorption peaks at ultraviolet-visible region.[S5, S6] For plasmonic metal-semiconductor composites, the SPR of metal component can boost the light harvesting and charge carrier migration of semiconductor.[S7-S10] Nonplasmonic Pt or Pd nanoparticles (with size < 20 nm) usually have relatively small cross-sections for surface plasmon, thus always exhibiting broad extinction from the ultraviolet to short-wavelength of visible light, without observable peaks.[S11] In addition, nonplasmonic Pt or Pd nanoparticles with low Fermi levels and strong interaction with hydrogen have been recognized as both effective co-catalysts and active sites that can be combined with semiconductor for proton reduction reactions.[S10, S12, S13]

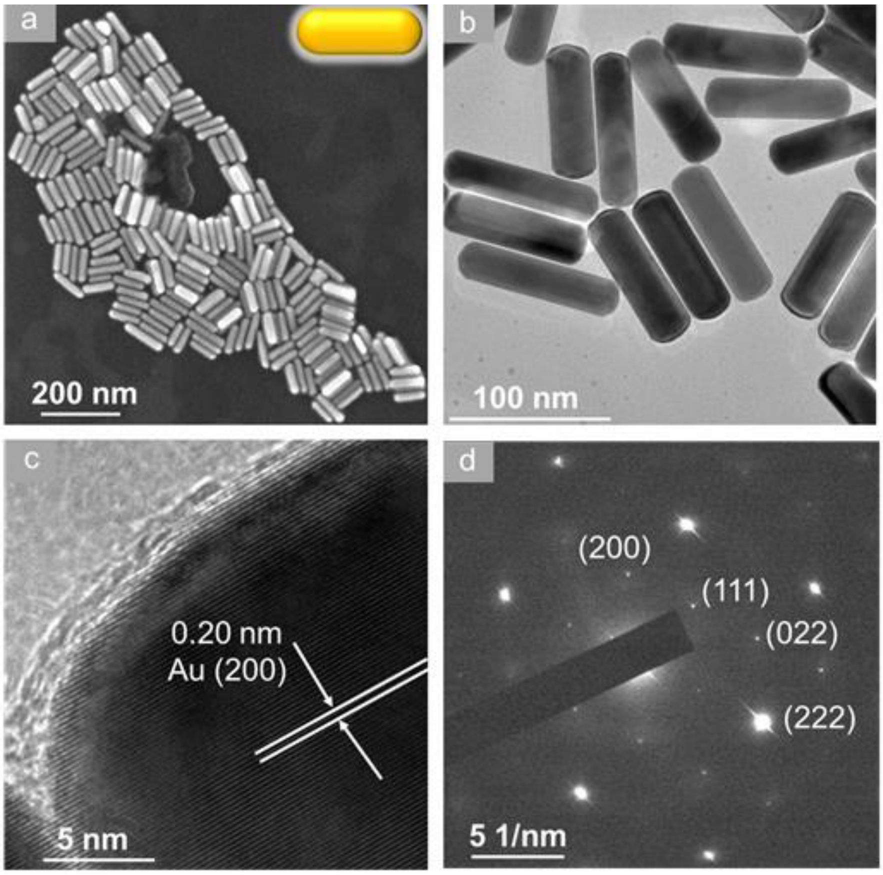

Fig. S1 (a) Scanning electron microscopy (SEM) image, (b) transmission electron microscopy (TEM) image, (c) high-resolution TEM (HRTEM) image and (d) selected area electron diffraction (SAED) pattern of Au nanorods (NRs). The inset of (a) shows structural model of Au NRs.

Note: From the SEM and TEM images in **Fig. S1a** and **b**, we can see that the resulting Au NRs have an average diameter of 29.0 nm and length of 92.5 nm with an aspect ratio of 3.2. The lattice fringes with a period of 0.20 nm can be well assigned to the (200) spacing of face-center cubic (fcc) Au (**Fig. S1c**). The SAED pattern (**Fig. S1d**) reflects the single crystalline structure of the Au NRs.

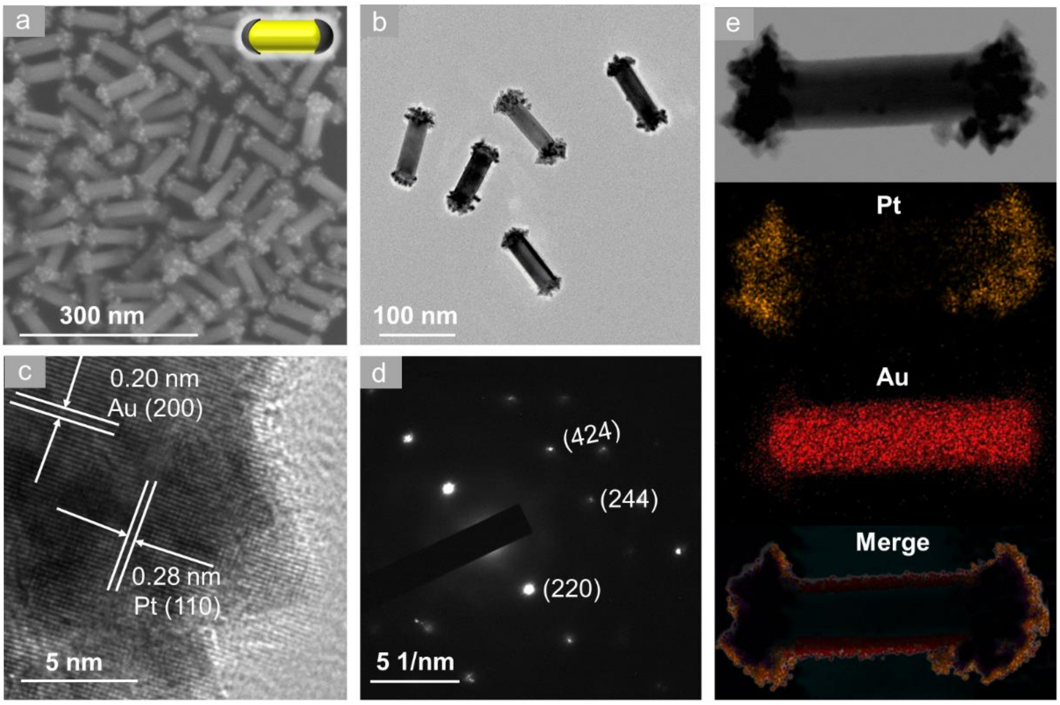

Fig. S2 (a) Scanning electron microscopy (SEM) image, (b) transmission electron microscopy (TEM) image, (c) high-resolution TEM (HRTEM) image, (d) selected area electron diffraction (SAED) pattern and (e) elemental mapping results of Pt-tipped Au (Au-Pt). The inset of (a) shows structural model of Au-Pt.

Note: As shown in **Fig. S2a-c**, after the growth of Pt onto the tips of Au nanorods (NRs), the smooth ends of Au NRs become rough, while the surface at the side of Au NRs remains almost unchanged. The average diameter at the middle of Au-Pt is 29.1 nm, which is similar to blank Au NRs (**Fig. S1a** and **b**), and the average length is increased to 114.0 nm. These results suggest that Pt tends to anisotropically deposit at the two ends of Au NRs. The lattice fringes with period of 0.20 nm and 0.28 nm can be assigned to the (200) spacing of face-center cubic (fcc) Au and the (110) spacing of fcc Pt, respectively (**Fig. S2c**). The SAED pattern (**Fig. S2d**) reflects the single crystalline structure of the Au-Pt. Elemental mapping analysis on Au-Pt (**Fig. S2e**) shows that the Pt is located at the tips of Au NRs, further confirming the tip-coated morphology of Au-Pt.

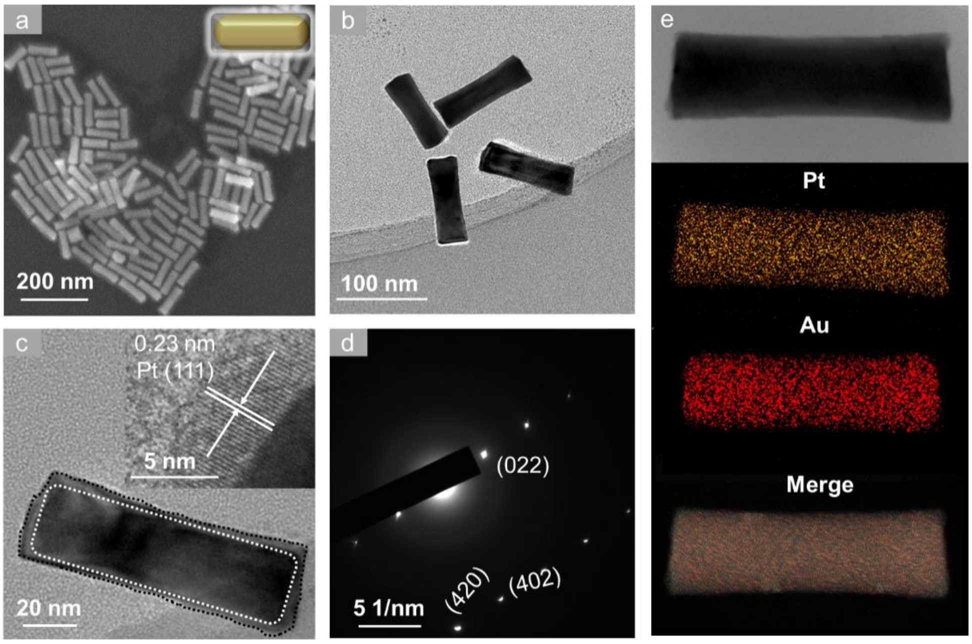

Fig. S3 (a) Scanning electron microscopy (SEM) image, (b and c) transmission electron microscopy (TEM) image, (d) selected area electron diffraction (SAED) pattern and (e) elemental mapping results of Pt-covered Au (Au@Pt). The inset of (a) shows the structural model of Au@Pt. The inset of (c) shows the high-resolution TEM (HRTEM) image of Au@Pt.

Note: As indicated by the SEM and TEM images in **Fig. S3a-c**, the resulting bar-like Au@Pt nanorods (NRs) have an average diameter of 33.2 nm and length of 107.9 nm with an aspect ratio of 3.3, which are enclosed by the Pt shell. The lattice fringes with a period of 0.23 nm can be well assigned to the (111) spacing of face-center cubic (fcc) Pt (inset of **Fig. S3c**). The shell thicknesses is about 2-7 nm based on the calculated size increment of Au@Pt NRs contrast to Au NRs (**Fig. S1**). The SAED pattern (**Fig. S3d**) reflects the single crystalline structure of the Au@Pt NRs with well-defined fcc structures. The structure composition information of Au@Pt is further supported by the elemental mapping analysis as displayed in **Fig. S3e**, in which the Pt shell is isotropically deposited on the entire surface of the Au NRs.

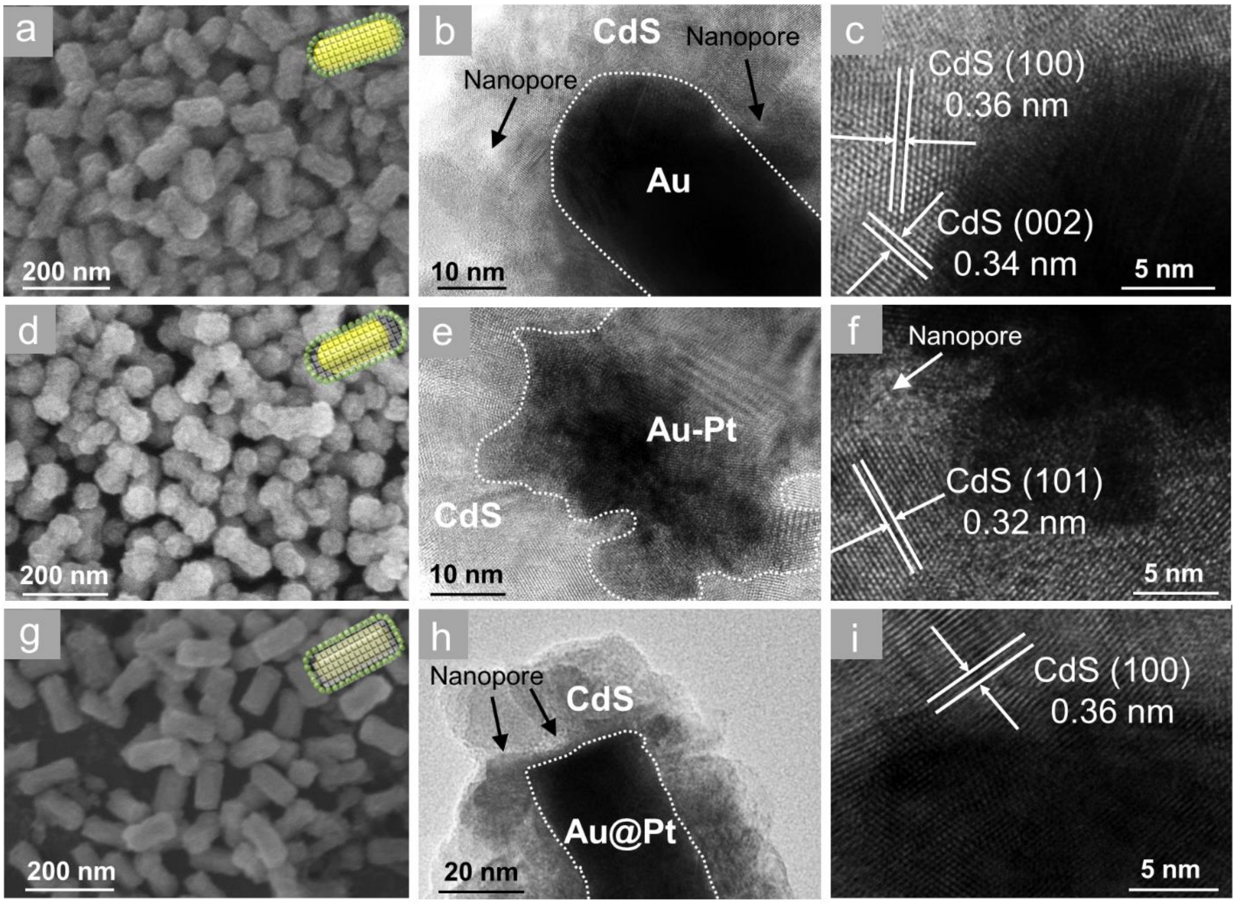

Fig. S4 (a) Scanning electron microscopy (SEM) image, (b) transmission electron microscopy (TEM) image and (c) high-resolution TEM (HRTEM) image of CdS deposited Au NRs (Au@CdS), (d) SEM image, (e) TEM image and (f) HRTEM image of CdS deposited Pt-tipped Au nanorods (Au-Pt@CdS), (g) SEM image, (h) TEM image, and (i) HRTEM image of CdS deposited Pt-covered Au NRs (Au@Pt@CdS). The insets of (a, d and g) show the corresponding structural models of the samples.

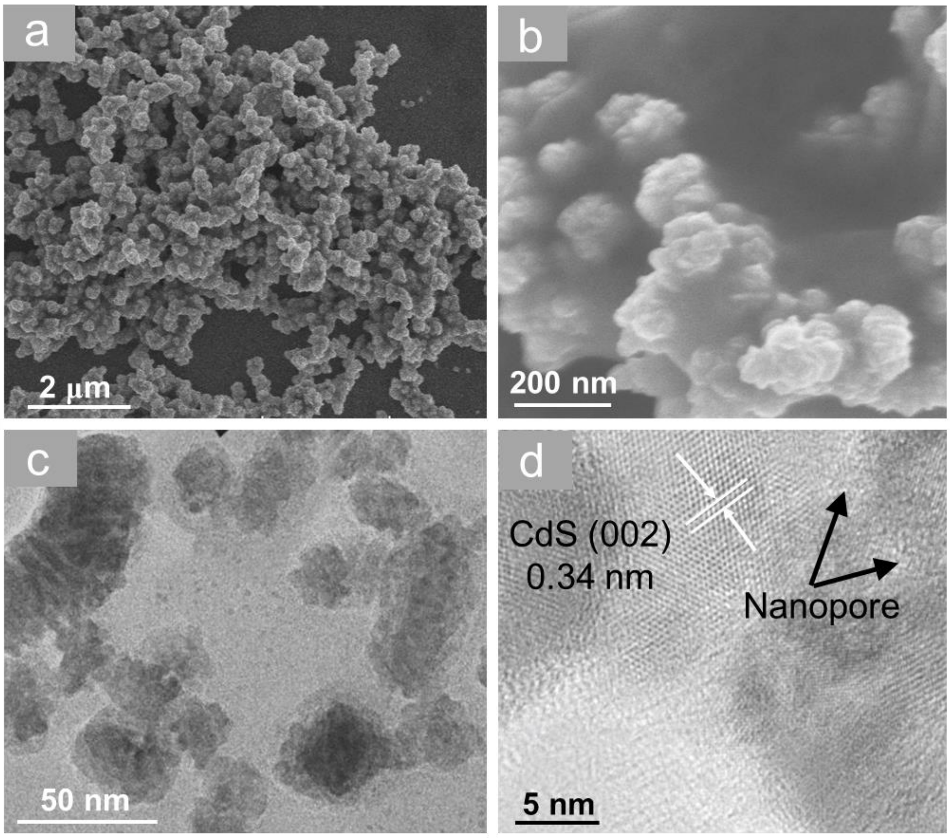

Fig. S5 (a and b) Scanning electron microscopy (SEM) images, (c) transmission electron microscopy (TEM) images and (d) high-resolution TEM (HRTEM) image of blank CdS.

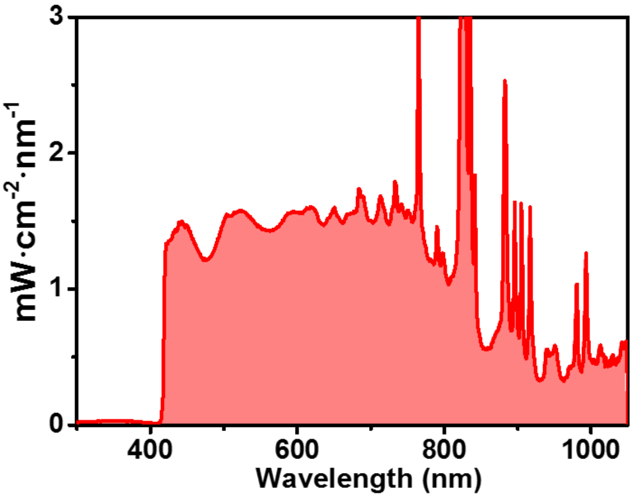

Fig. S6 The spectrum of irradiation source (λ > 420 nm) used in the photocatalysis experiments.

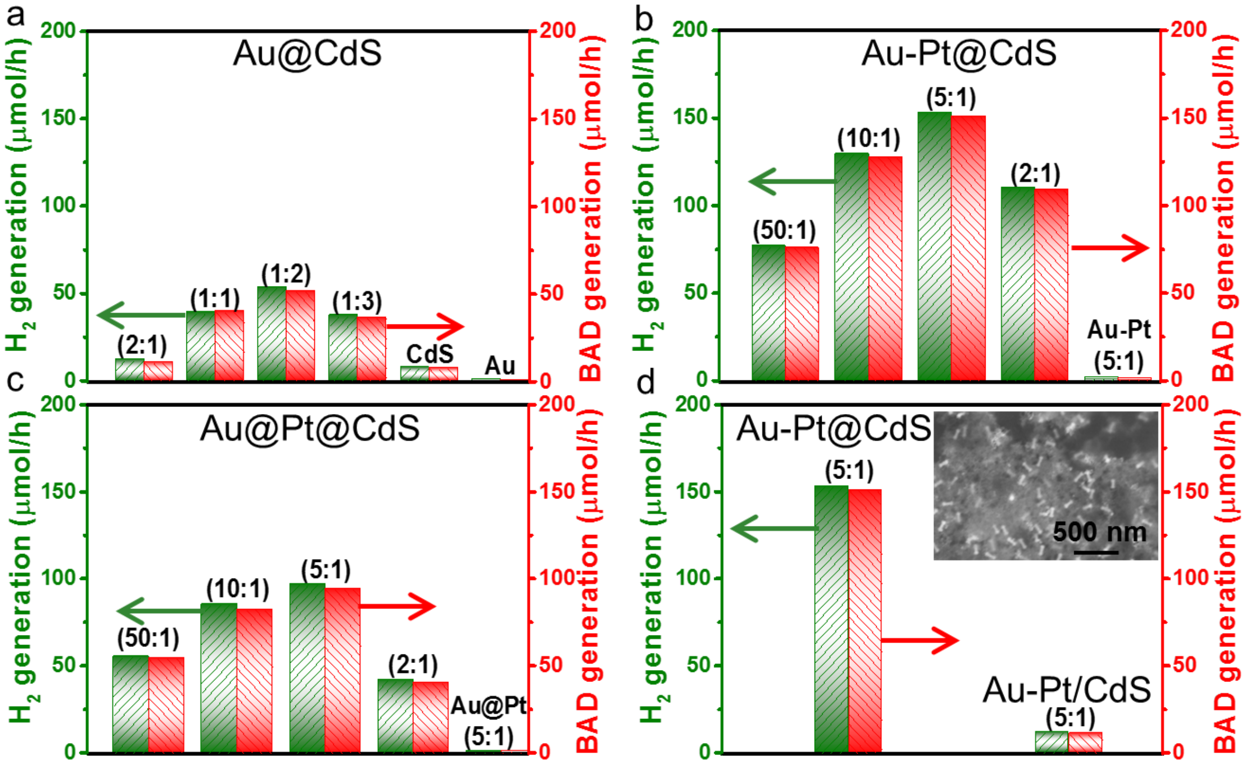

Fig. S7 H_2 and benzaldehyde (BAD) production rates in photocatalytic conversion of benzyl alcohol (BA) under visible-near-infrared (Vis-NIR) light (λ > 420 nm) irradiation using (a) blank CdS, Au, and CdS deposited Au nanorods (Au@CdS) with different Au:CdS mass ratios, (b) blank Au-Pt and CdS deposited anisotropic Pt-tipped Au nanorods (Au-Pt@CdS) with different Au:Pt mass ratios, (c) blank Au@Pt and CdS deposited isotropic Pt-covered Au nanorods (Au@Pt@CdS) with different Au:Pt mass ratios and (d) Au-Pt@CdS and CdS supported Au-Pt NRs (Au-Pt/CdS) with the Au:Pt mass ratios at 5:1. The inset of (d) shows the scanning electron microscopy (SEM) image of Au-Pt/CdS. In (b-d), the Au:CdS mass ratios were fixed at 1:2. The numbers in brackets of (a-d) represent the corresponding mass ratios.

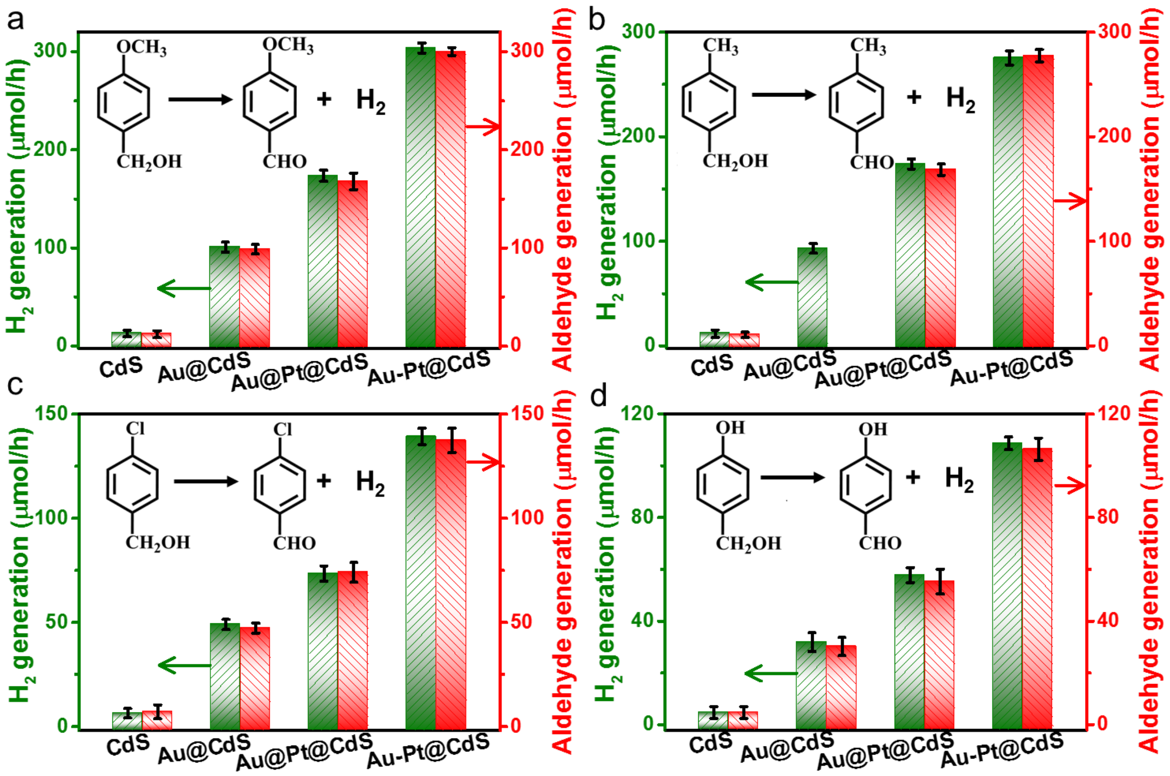

Fig. S8 (a-d) H_2 and aldehydes production rates in photocatalytic conversion of different aromatic alcohols (R-PhCH_2OH, R = OCH_3, CH_3, Cl and OH) under visible-near-infrared (Vis-NIR) light (λ > 420 nm) irradiation over CdS and metal-CdS hybrids. Error bars represent the standard deviation from three repeated measurements. The insets of (a-d) show the formulas for photocatalytic conversion of aromatic alcohols to aldehydes and H_2.

Table S1 Comparison of other similar coupled reaction systems for simultaneous H_2 and value-added chemicals production in the presence of different biomass-derived substrates.

Materials	Activity (mmol $g^{-1}h^{-1}$)$^{a)}$	Selectivity$^{b)}$	AQY	Substrate	Ref.
Au-Pt@CdS	76.5	94.0%	19.3% at 450 nm	Benzyl alcohol	This work
Au@Pt@CdS	48.3	94.6%	16.7% at 450 nm	Benzyl alcohol	This work
Pt/PCN-777	ca. 0.3	99.0%	—	Benzylamine	S14
P-$Zn_xCd_{1-x}S$	ca. 0.4	65.0%	0.12% under white LED	5-hydroxymethyl furfural	S15
CN_x–NiP	ca. 0.8	99.0%	15% at 360 nm	4-methylbenzyl alcohol	S16
Pd-CdS-TiO_2	1.2	99.0%	3.5% at 480 nm	Benzyl alcohol	S17
Ni-CdS	8.9	100%	—	5-hydroxymethyl furfural	S18
TiO_2	16.9	83.6%	—	Ethanol	S19
Ni-CdS	46.6	100%	48% at 447 nm	2-propanol	S20
Pd-TiO_2	51.5	92.0%	5.3% at 365 nm	Ethanol	S21
Co-CdS	169.7	66.8%	63.2% at 420 nm	Benzyl alcohol	S22

a) Referring to H_2 production rate; b) Referring to the selectivity for value-added oxidation product.

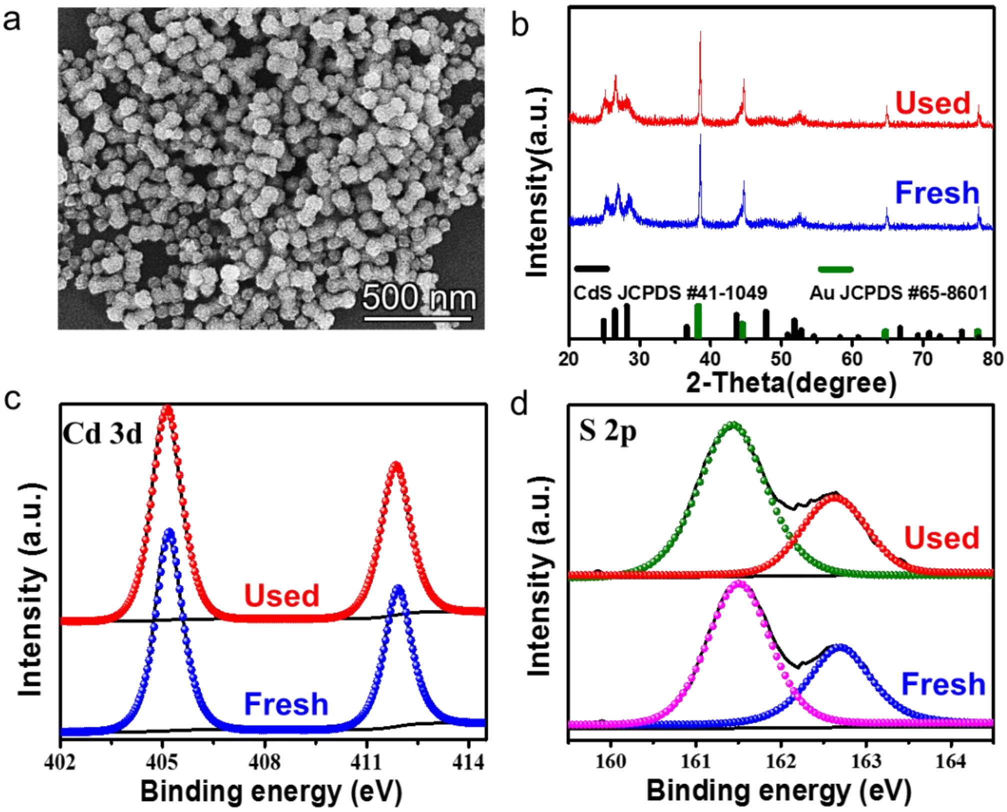

Fig. S9 (a) Scanning electron microscopy (SEM) image of used CdS deposited anisotropic Pt-tipped Au nanorods (Au-Pt@CdS). (b) X-ray diffraction (XRD) patterns of used and fresh Au-Pt@CdS. X-ray photoelectron spectroscopy (XPS) spectra of (c) Cd 3d and (d) S 2p for used and fresh Au-Pt@CdS.

Note: To learn whether there are changes in the morphology, composition and structure of Au-Pt@CdS sample after reactions, the fresh and used photocatalysts were characterized by SEM, XRD and XPS. SEM image in **Fig. S9a** indicates a well maintained nanorod structure of the used Au-Pt@CdS. Furthermore, XRD patterns (**Fig. S9b**) of the samples reveal intact crystalline structure of hexagonal phases CdS for the composite after recycling photocatalytic reactions.[S6, S23] The photostability of Au-Pt@CdS can also be deduced from the XPS data. In **Fig. S9c** and **S9d**, both Cd 3d and S 2p XPS spectra of used Au-Pt@CdS sample exhibit signatures attributed to the bulk CdS.[S6, S24] The peak intensity and binding energy of Cd and S in the fresh and used samples are almost identical. In addition, there is no detectable Cd^{2+} leaching in the reaction solution, as confirmed by inductively coupled plasma (ICP) detection analysis. The above results indicate no significant photo-corrosion of CdS after long-term photocatalytic reaction. The photostability of Au-Pt@CdS could be ascribed to the efficient charge transfer and surface redox reactions.[S17, S23, S25]

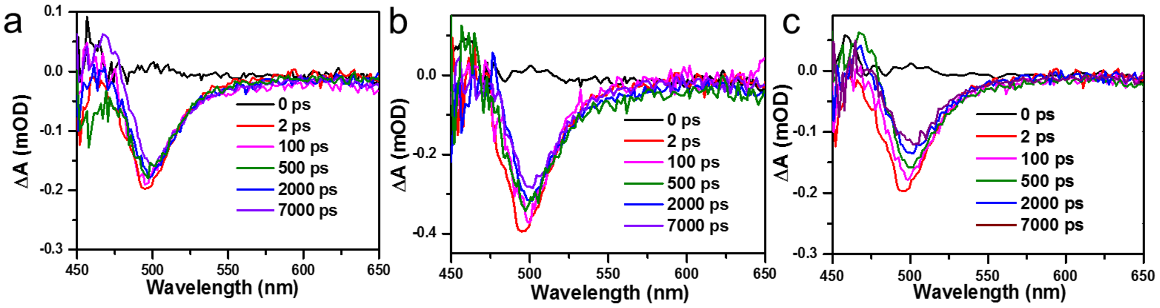

Fig. S10 Transient absorption (TA) spectra of (a) CdS, (b) CdS deposited Au nanorods (Au@CdS) and (c) CdS deposited isotropic Pt-covered Au nanorods (Au@Pt@CdS) with time delays after 370 nm excitation.

Equation S1-3:

$$I\,(t) = A_1 \exp\,(-t\,/\tau_1) + A_2 \exp\,(-t\,/\tau_2) \qquad (1)$$

$$\tau_{\mathrm{A}} = \frac{A_1\tau_1{}^2 + A_2\tau_2{}^2}{A_1\tau_1 + A_2\tau_2} \qquad (2)$$

$$k_{\mathrm{ct}} = \frac{1}{\tau_{\mathrm{A}}} \qquad (3)$$

Table S2 Transient absorption (TA) decay dynamics analysis for CdS and metal-CdS hybrids.

Samples	A_1 (%)	τ_1 (ns)	A_2 (%)	T_2 (ns)	T_A (ns)	k_{ct} (ns^{-1})
CdS	97.0	16.0	3.0	1.5	16.0	0.06
Au@CdS	66.5	14.1	33.5	0.6	13.9	0.07
Au@Pt@CdS	67.7	4.4	32.3	0.3	4.3	0.2
Au-Pt@CdS	62.2	2.5	37.8	0.2	2.4	0.4

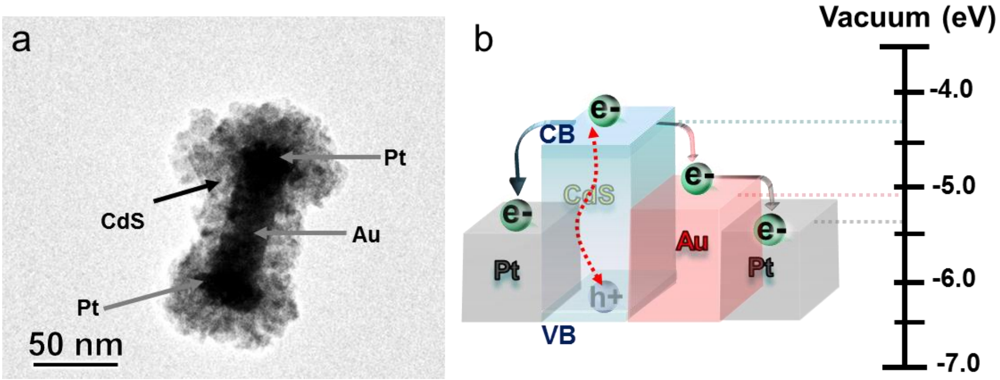

Fig. S11 (a) Transmission electron microscopy (TEM) image shows the direct and multiple metal-semiconductor and metal-metal interfacial contact in CdS deposited anisotropic Pt-tipped Au nanorods (Au-Pt@CdS). (b) Schematic illustration of the energy band alignment and multichannel electrons transfer in Au-Pt@CdS heterostructures. CB and VB represent the conduction band and valence band, respectively.

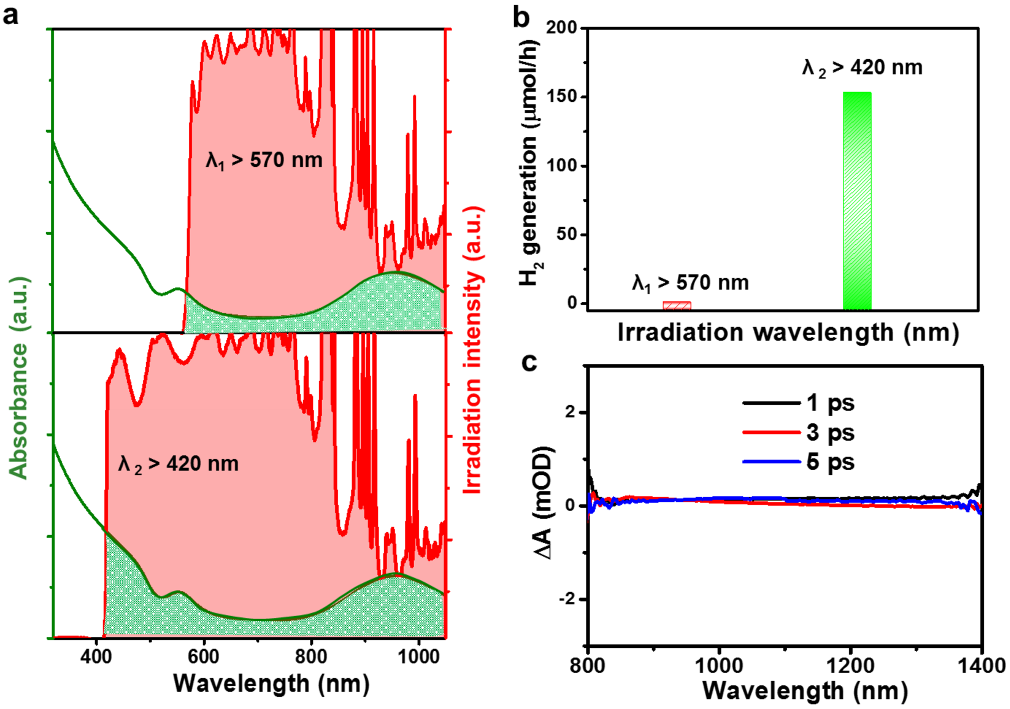

Fig. S12 (a) Wavelength-control experiments under visible-near-infrared (Vis-NIR) light λ > 570 nm and λ > 420 irradiation over the optimal CdS deposited anisotropic Pt-tipped Au nanorods (Au-Pt@CdS) and (b) the corresponding H_2 production rate in photocatalytic conversion of benzyl alcohol (BA). The green area in (a) show the spectrum overlap between irradiation source (red curve) and absorbance of Au-Pt@CdS (green curve). (c) Transient absorption (TA) spectra of Au-Pt@CdS with time delays after 570 nm excitation.

Note: To investigate the possible impacts of hot electrons transfer from metal to semiconductor CdS on the photoactivity enhancement, we performed the control experiment over Au-Pt@CdS under long-wavelength Vis-NIR light (λ > 570 nm) irradiation (**Fig. S12a**). Under such conditions, the band-gap photoexcitation of semiconductor CdS can be prevented so that the hot electrons transfer effects of plasmonic Au-Pt in the composites are exclusively studied.[S4, S6, S26] It is seen from **Fig. S12b** that the Au-Pt@CdS hybrids show only trace photoactivity although it has the significant surface plasmon resonance (SPR) absorption of bimetallic Au-Pt, indicating that the effect of SPR-excited hot electrons injection from Au-Pt to CdS on the photoactivity enhancement is negligible.[S27, S28] When we used the photon energy at 570 nm to excite the T-SPR of Au-Pt@CdS in TA measurement, the sample shows no signal corresponding to excitation and relaxation kinetics (**Fig. S12c**), which further confirms the absence of hot electrons transfer process. Thus, the SPR enhancement mechanisms should be interpreted in terms of electric field effect.[S29]

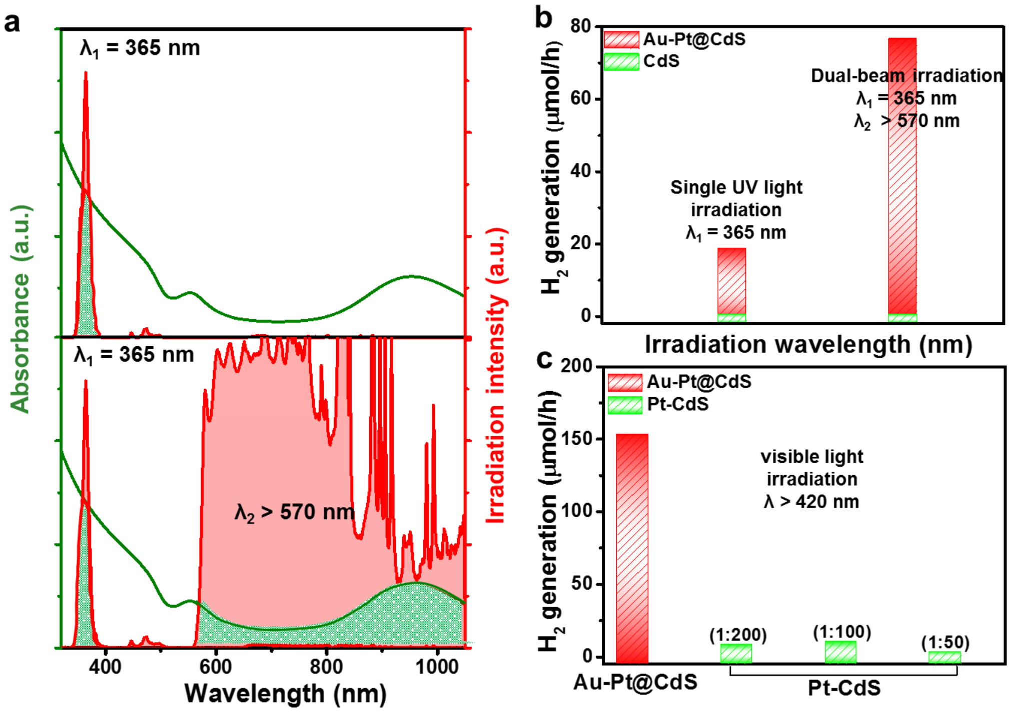

Fig. S13 (a) Wavelength-control experiments under single ultraviolet (UV) light (λ = 365 nm) and dual-beam UV light with additional Vis-NIR light (λ > 570 nm) irradiation over CdS and the optimal CdS deposited anisotropic Pt-tipped Au nanorods (Au-Pt@CdS) and (b) the corresponding H_2 production rate in conversion of benzyl alcohol (BA). The green area in (a) show the spectrum overlap between irradiation source (red curve) and absorbance of Au-Pt@CdS (green curve). (c) H_2 production rates in photocatalytic conversion of BA under Vis-NIR light (λ > 420 nm) irradiation over Au-Pt@CdS and Pt-loaded CdS catalyst (Pt-CdS) with different Pt:CdS mass ratios. The numbers in brackets of (c) represent the corresponding mass ratios.

Note: Control experiments under UV light (λ = 365 nm) with additional Vis-NIR light (λ > 570 nm) illumination (**Fig. S13a**) were performed to further examine the contributions of the possible SPR excitation of Au-Pt to the photoactivity of Au-Pt@CdS.[S30-S32] The λ = 365 nm light mainly induces the band-gap excitation of semiconductor CdS, while the λ > 570 nm light matches the SPR absorption of bimetallic Au-Pt. As shown in **Fig. S13b**, the Au-Pt@CdS exhibits enhanced photoactivity as compared to bare CdS under single-beam UV light irradiation. Since the SPR of Au-Pt is weak under UV light irradiation,[S33-S35] the photoactivity enhancement of Au-Pt@CdS sample should be originated from the co-catalysts effect of Au-Pt that accept the photoinduced electrons from the deposited CdS.[S33, S34] In addition, no obvious change in H_2 evolution rate can be observed for blank CdS under dual-beam light irradiation as compared to single-beam UV light irradiation, indicating that the effect of secondary irradiation of λ > 570 nm light on H_2 formation is negligible for CdS. In contrast, the H_2 evolution rate over Au-Pt@CdS exhibits further enhancement under the secondary irradiation to drive the electric field enhancement. We also prepared nonplasmonic Pt-loaded CdS catalysts (Pt-CdS) through the well-reported photodeposition method.[S22, S30] The optimal H_2 production rate under Vis-NIR light irradiation over Pt-CdS sample is 10.1 μmol h^{-1} (**Fig. S13c**), which is much lower than that over plasmonic Au-Pt@CdS (153.0 μmol h^{-1}). The above joint results signify that the promoted photoactivity of Au-Pt@CdS is induced by the synergistic coupling of the band-gap photoexcitation of semiconductor CdS with the electric field enhancement and the co-catalysts effect of Au-Pt bimetal.[S30-S32]

Table S3 Charge carrier density (N_D) analysis for CdS and metal-CdS hybrids.

Samples	N_D (10^{17}cm^{-3})
CdS	2.1
Au@CdS	2.3
Au@Pt@CdS	3.0
Au-Pt@CdS	4.6

References

S1 P. Zhang, T. Wang and J. Gong, *Adv. Mater.*, 2015, **27**, 5328-5342.

S2 N. Zhang, C. Han, X. Fu and Y.-J. Xu, *Chem*, 2018, **4**, 1832-1861.

S3 C. Wang and D. Astruc, *Chem. Soc. Rev.*, 2014, **43**, 7188-7216.

S4 Y.-C. Pu, G. Wang, K.-D. Chang, Y. Ling, Y.-K. Lin, B. C. Fitzmorris, C.-M. Liu, X. Lu, Y. Tong and J. Z. Zhang, *Nano Lett.*, 2013, **13**, 3817-3823.

S5 S. T. Kochuveedu, Y. H. Jang and D. H. Kim, *Chem. Soc. Rev.*, 2013, **42**, 8467-8493.

S6 C. Han, Q. Quan, H. M. Chen, Y. Sun and Y.-J. Xu, *Small*, 2017, **13**, 1602947.

S7 L. Ma, S. Liang, X.-L. Liu, D.-J. Yang, L. Zhou and Q.-Q. Wang, *Adv. Funct. Mater.*, 2015, **25**, 898-904.

S8 L. Ma, K. Chen, F. Nan, J.-H. Wang, D.-J. Yang, L. Zhou and Q.-Q. Wang, *Adv. Funct. Mater.*, 2016, **26**, 6076-6083.

S9 Z. W. Seh, S. Liu, M. Low, S. Y. Zhang, Z. Liu, A. Mlayah and M. Y. Han, *Adv. Mater.*, 2012, **24**, 2310-2314.

S10 S.-F. Hung, Y.-C. Yu, N.-T. Suen, G.-Q. Tzeng, C.-W. Tung, Y.-Y. Hsu, C.-S. Hsu, C.-K. Chang, T.-S. Chan, H.-S. Sheu, J.-F. Lee and H. M. Chen, *Chem. Commun.*, 2016, **52**, 1567-1570.

S11 N. Zhang, C. Han, Y.-J. Xu, J. J. Foley IV, D. Zhang, J. Codrington, S. K. Gray and Y. Sun, *Nature Photon.*, 2016, **10**, 473-482.

S12 S. Bai, X. Li, Q. Kong, R. Long, C. Wang, J. Jiang and Y. Xiong, *Adv. Mater.*, 2015, **27**, 3444-3452.

S13 A. A. Melvin, K. Illath, T. Das, T. Raja, S. Bhattacharyya and C. S. Gopinath, *Nanoscale*, 2015, **7**, 13477-13488.

S14 L. Hang, X. Caiyun, L. Dandan and J. Hai-Long, *Angew. Chem. Int. Ed.*, 2018, **57**, 5379-5383.

S15 H.-F. Ye, R. Shi, X. Yang, W.-F. Fu and Y. Chen, *Appl. Catal. B*, 2018, **233**, 70-79.

S16 H. Kasap, C. A. Caputo, B. C. M. Martindale, R. Godin, V. W.-h. Lau, B. V. Lotsch, J. R. Durrant and E. Reisner, *J. Am. Chem. Soc.*, 2016, **138**, 9183-9192.

S17 S. Higashimoto, Y. Tanaka, R. Ishikawa, S. Hasegawa, M. Azuma, H. Ohue and Y. Sakata, *Catal. Sci. Technol.*, 2013, **3**, 400-403.

S18 G. Han, Y.-H. Jin, R. A. Burgess, N. E. Dickenson, X.-M. Cao and Y. Sun, *J. Am. Chem. Soc.*, 2017, **139**, 15584-15587.

S19 H. Lu, J. Zhao, L. Li, L. Gong, J. Zheng, L. Zhang, Z. Wang, J. Zhang and Z. Zhu, *Energy Environ. Sci.*, 2011, **4**, 3384-3388.

S20 Z. Chai, T.-T. Zeng, Q. Li, L.-Q. Lu, W.-J. Xiao and D. Xu, *J. Am. Chem. Soc.*, 2016, **138**, 10128-10131.

S21 B. Weng, Q. Quan and Y.-J. Xu, *J. Mater. Chem. A*, 2016, **4**, 18366-18377.

S22 D. Jiang, X. Chen, Z. Zhang, L. Zhang, Y. Wang, Z. Sun, R. M. Irfan and P. Du, *J. Catal.*, 2018, **357**, 147-153.

S23 C. Han, Z. Chen, N. Zhang, J. C. Colmenares and Y. J. Xu, *Adv. Funct. Mater.*, 2015, **25**, 221-229.

S24 X. Ma, K. Zhao, H. Tang, Y. Chen, C. Lu, W. Liu, Y. Gao, H. Zhao and Z. Tang, *Small*, 2014, **10**, 4664-4670.

S25 G. Xie, K. Zhang, B. Guo, Q. Liu, L. Fang and J. R. Gong, *Adv. Mater.*, 2013, **25**, 3820-3839.

S26 D. B. Ingram and S. Linic, *J. Am. Chem. Soc.*, 2011, **133**, 5202-5205.

S27 J. Li, S. K. Cushing, J. Bright, F. Meng, T. R. Senty, P. Zheng, A. D. Bristow and N. Wu, *ACS Catal.*, 2013, **3**, 47-51.

S28 S. K. Cushing, J. Li, F. Meng, T. R. Senty, S. Suri, M. Zhi, M. Li, A. D. Bristow and N. Wu, *J. Am. Chem. Soc.*, 2012, **134**, 15033-15041.

S29 J. Xu, W.-M. Yang, S.-J. Huang, H. Yin, H. Zhang, P. Radjenovic, Z.-L. Yang, Z.-Q. Tian and J.-F. Li, *Nano Energy*, 2018, **49**, 363-371.

S30 A. Tanaka, K. Hashimoto and H. Kominami, *J. Am. Chem. Soc.*, 2014, **136**, 586-589.

S31 Z. Zhang, A. Li, S.-W. Cao, M. Bosman, S. Li and C. Xue, *Nanoscale*, 2014, **6**, 5217-5222.

S32 Y.-H. Chiu, K.-D. Chang and Y.-J. Hsu, *J. Mater. Chem. A*, 2018, **6**, 4286-4296.
S33 L. Yuan, B. Weng, J. C. Colmenares, Y. Sun and Y.-J. Xu, *Small*, 2017, **13**, 1702253.
S34 Z. Zhang, Y. Huang, K. Liu, L. Guo, Q. Yuan and B. Dong, *Adv. Mater.*, 2015, **27**, 5906-5914.
S35 H. Li, F. Qin, Z. Yang, X. Cui, J. Wang and L. Zhang, *J. Am. Chem. Soc.*, 2017, **139**, 3513-3521.